GEOPHYSICS, VOL. 64, NO. 6 (NOVEMBER-DECEMBER 1999); P. 1939–1948, 23 FIGS.

Apparent AVA effects of fine layering

Kees Wapenaar*, Aart-Jan van Wijngaarden‡, Wim van Geloven**, and Taco van der Leij§

ABSTRACT

The fine layering of the earth's subsurface causes apparent amplitude-variation-with-angle (AVA) effects in seismic reflection data. One can distinguish between reflection- and propagation-related apparent AVA effects: the reflection of a package of thin layers is accompanied with angle-dependent wavelet interference, whereas propagation through finely layered media causes angle-dependent wavelet dispersion. Obviously, both types of apparent AVA effects hinder AVA inversion for the elastic parameters.

Due to the band limitation of the seismic data, the reflection-related interference effects cannot be removed. However, they can be equalized for all propagation angles by applying an angle-dependent filter in the imaging step in angle-dependent migration schemes. The underlying assumption is that the source function is known and that source directivity effects have been compensated prior to migration. The propagation-related dispersion effects can be compensated for in the downward extrapolation process by means of inverse generalized primary propagators.

Angle-dependent migration, including the above mentioned modifications, yields an angle-dependent reflectivity section in which the apparent AVA effects of fine layering are suppressed.

INTRODUCTION

The relation between the angle-dependent reflectivity of an interface in a target zone and the amplitude-variation-with-offset (AVO) effects observed in the seismic data at the surface is complicated by many factors (Ostrander, 1984; Swan, 1991). Some of these factors are "reflection related" (such as thin-bed tuning, reflector curvature), others "propagation related" (such as geometrical spreading, transmission and/or anelastic losses) or "acquisition related" (such as source/receiver directivity, geophone coupling).

In this paper, we address the reflection and propagation related apparent amplitude-variation-with-angle (AVA) effects of fine layering, and we propose a method that compensates for these effects in migration. The main steps in migration are downward extrapolation and imaging. The reflection-related apparent AVA effects will be suppressed with an improved imaging procedure, whereas an improved downward extrapolation scheme will compensate for the propagation-related apparent AVA effects.

REFLECTION-RELATED AVA EFFECTS OF FINE-LAYERING

The reflection-related apparent AVA effects of fine layering are best illustrated by considering the primary plane-wave response of an acoustic, horizontally layered, constant velocity ($c = 2000$ m/s), variable density medium (see Figure 1). Since for this situation the reflectivity of each individual interface is angle independent, any apparent AVA will show up immediately. Figure 2 shows an image in the raypath parameter–depth (p, z) domain. This image has been obtained by 1-D angle-dependent migration (downward extrapolation and imaging per raypath parameter p; see, for example, Clayton and McMechan, 1981) but the same result could have been obtained by a simple time-to-depth conversion, according to $z = c\tau/(2\cos\phi)$, where τ is the intercept time and ϕ the propagation angle (with $\cos\phi = \sqrt{1 - c^2 p^2}$). Figure 3 shows the picked amplitudes at $z = 157$ m. Note that both Figures 2 and 3 clearly exhibit AVA behavior, despite the fact that the local reflection function is angle independent. Needless to say, a

Presented at the 65th Annual International Meeting, Society of Exploration Geophysicists. Manuscript received by the Editor April 1, 1996; revised manuscript received April 29, 1998.
*Delft University of Technology, Centre for Technical Geoscience, Lab of Seismics and Acoustics, Lorentzweg 1, 2628 CJ Delft, Netherlands. E-mail: c.p.a.wapenaar@ ctg.tudelft.nl.
‡Formerly Delft University of Technology, Centre for Technical Geoscience; presently Norsk Hydro, Sandsliveien 90, Bergen, Norway. E-mail: aart.jan.van.wijngaarden@hydro.com.
**Formerly Delft University of Technology, Centre for Technical Geoscience; presently DTO Maasland, Coldenhovelaan 1, 3155 RC Maasland, Netherlands. E-mail: wjf.v_geloven@ dcc.disp.mindef.nl.
§Formerly Delft University of Technology, Centre for Technical Geoscience; presently Arthur D. Little International Inc., P.O. Box 540, 3000 AM Rotterdam, Netherlands. E-mail: vanderleij.taco@adlittle.com.

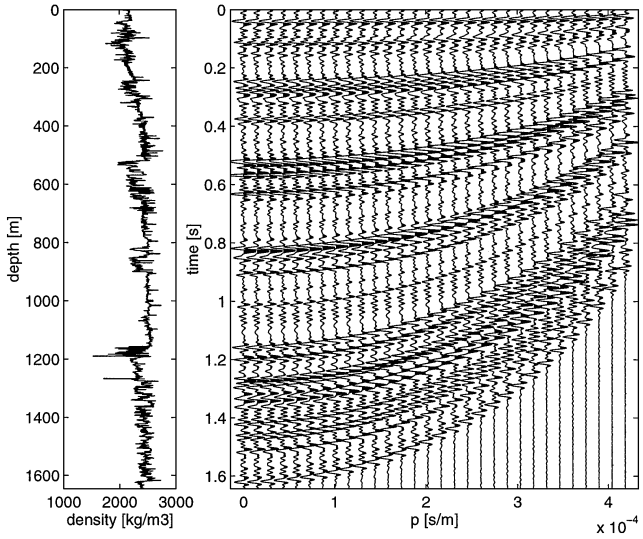

FIG. 1. Density log of a finely layered constant velocity medium ($c = 2000$ m/s) and the corresponding primary plane-wave reflection response (modeled with the reflectivity method, using a zero-phase wavelet with central frequency $f_c = 50$ Hz).

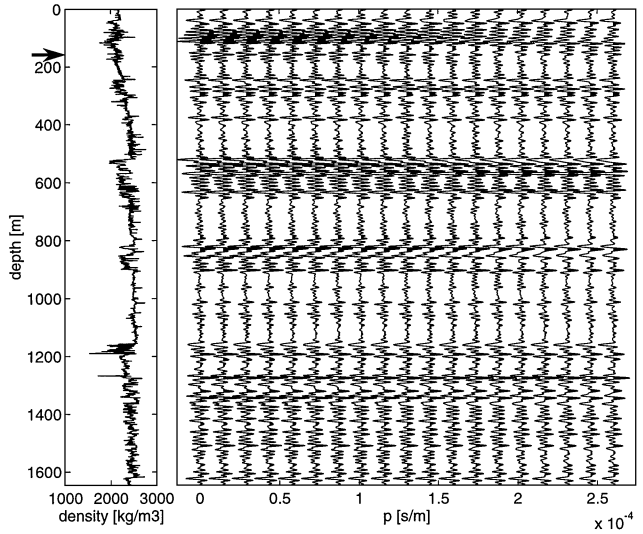

FIG. 2. Reflectivity section obtained with standard 1-D angle-dependent migration. Note the apparent AVA behavior.

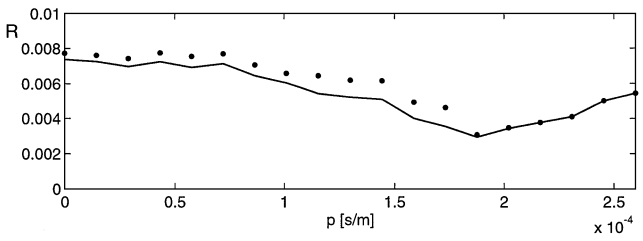

FIG. 3. Amplitude cross-sections. Solid: picked amplitudes exactly at $z = 157$ m; dotted: picked maximum amplitudes in a small depth interval around $z = 157$ m. Note the apparent AVA behavior (the relatively low amplitudes are due to the fact that the reflectivity section in Figure 2 is band limited).

local inversion of the AVA curve (see, for example, de Haas and Berkhout, 1990; van Wijngaarden, 1998) would lead to erroneous medium parameters.

Compensating for reflection-related apparent AVA

The apparent AVA behavior observed in Figures 2 and 3 is a result of angle-dependent interference, which is easily explained with the aid of Figure 4. This figure shows two plane waves illuminating the medium under two different angles. The frequency ω is the same for both angles. As a result, the vertical wavelength λ_z in the right frame is different from the wavelength λ in the left frame. In other words, for different illumination angles, the medium is observed at different scales. This can be cured by choosing different frequencies ω at different angles, such that the vertical wavelength λ_z remains constant (Figure 5). For a constant velocity medium, λ_z and ω are related according to

$$\lambda_z = \frac{2\pi c}{\omega \cos\phi} = \frac{2\pi c}{\omega\sqrt{1 - c^2 p^2}}. \tag{1}$$

Hence, in order to make λ_z independent of the propagation angle ϕ, the frequency ω should be chosen such that $\omega \cos\phi$ is constant. For broad-band data, a similar effect is obtained by applying a p-dependent filter with a frequency passband defined by

$$\omega_\ell(p) < \omega < \omega_u(p), \tag{2}$$

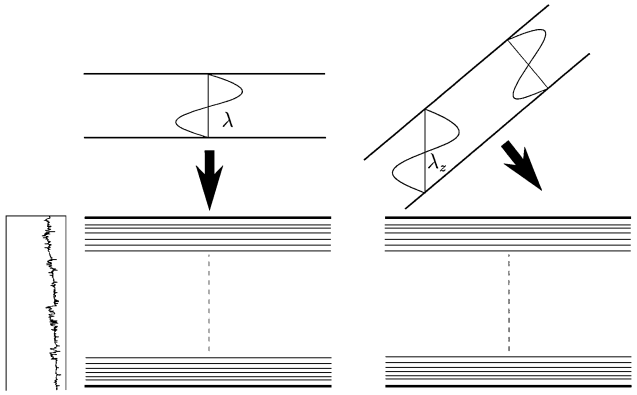

FIG. 4. For different angles and the same ω, $\lambda_z \neq \lambda$.

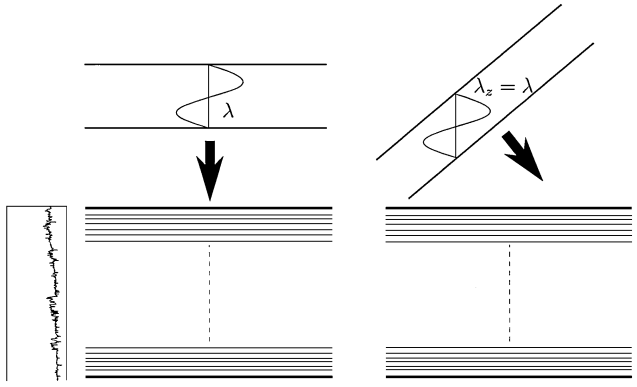

FIG. 5. For different angles and different ω, $\lambda_z = \lambda$.

such that $\omega_\ell(p)\cos\phi(p)=\omega_1$ and $\omega_u(p)\cos\phi(p)=\omega_2$. Here, ω_1 and ω_2 are constants that can be chosen freely, with the constraint that $\omega_\ell(p)$ and $\omega_u(p)$ do not exceed the band limits of the seismic data for the considered p-values. Note that this pass-band filter can be applied to the data in the (p,ω)-domain before migration, or it can be integrated in the imaging step in angle-dependent migration, according to

$$\langle\tilde{R}(p,z)\rangle=\frac{\mathcal{C}(p)}{\pi}\Re\int_{\omega_\ell(p)}^{\omega_u(p)}\left(\frac{\tilde{P}(p,z,\omega)}{S(\omega)}\right)\mathrm{d}\omega. \quad (3)$$

Here $\tilde{P}(p,z,\omega)$ denotes the downward extrapolated data at depth z in the raypath parameter–frequency domain, $S(\omega)$ the source function, and $\mathcal{C}(p)$ a weighting factor. Moreover, $\Re$ denotes that the real part is taken and $\langle\tilde{R}(p,z)\rangle$ denotes the imaged reflectivity. The latter approach has the advantage that it can be easily generalized to more realistic situations, as we will see later.

In Appendix A, it is shown that by defining the weighting factor as $\mathcal{C}(p)=2\cos\phi(p)/c$, the imaging result $\langle\tilde{R}(p,z)\rangle$ can be written as

$$\langle\tilde{R}(p,z)\rangle=b(z)\ *\ \tilde{R}(p,z) \quad (4)$$

[equation (A-6)]. Here $*$ denotes convolution along the z-axis, $\tilde{R}(p,z)$ the true reflectivity, and $b(z)$ denotes a spatial wavelet that is independent of the raypath parameter p. Hence, by applying the imaging step according to equation (3), the imaged result has a constant spatial bandwidth, which means that the interference effects are equalized. Optionally, a replacement source function $S_r(\omega\mathcal{C}(p))$ can be inserted under the integral in equation (3) in order to suppress the artifacts of the division by $S(\omega)$. In that case, the spatial wavelet $b(z)$ in equation (4) is given by the inverse Fourier transform of $S_r(k_z)$ [see equation (A-11)].

Note that the proposed imaging procedure (equation 3) is based on the assumption that the source function $S(\omega)$ is known and contains no directivity effects. In practice, this situation is achieved by applying adaptive surface-related multiple elimination and directional deconvolution prior to migration (Verschuur et al., 1992; Prein and Verschuur, 1997). Also note that no a priori assumptions are made on the parameterization of $\tilde{R}(p,z)$ [for comparison, Swan (1997) attacks the offset-dependent tuning problem, using a linearized Zoeppritz approximation of $\tilde{R}(p,z)$].

We applied 1-D angle-dependent migration to the data of Figure 1, using the imaging integral defined by equation (3) (see Figures 6 and 7). Note that the apparent AVA effects have been removed completely at the cost of some loss of resolution at the small propagation angles. For $p=0$, the bandwidth is reduced approximately by a factor $\cos\phi_{max}=\sqrt{1-c^2p_{max}^2}$. Hence, for a maximum propagation angle of 30°, we have $\cos\phi_{max}=\sqrt{3/4}\approx 0.87$, which means that the resolution loss for vertical propagation is 13%. Van Wijngaarden and Wapenaar (1995) discuss how to reduce this resolution loss.

Extension to acoustic variable-velocity media

In the previous subsection, we considered a constant velocity medium. When the velocity is varying as a function of z, we obtain similar results if we modify equation (3) to

$$\langle\tilde{R}(p,z)\rangle=\frac{\mathcal{C}(p,z)}{\pi}\Re\int_{\omega_\ell(p,z)}^{\omega_u(p,z)}\left(\frac{\tilde{P}(p,z,\omega)}{S(\omega)}\right)\mathrm{d}\omega, \quad (5)$$

with

$$\mathcal{C}(p,z)=2\cos\bar{\phi}(p,z)/\bar{c}(z), \quad (6)$$

$$\omega_\ell(p,z)=\omega_1/\cos\bar{\phi}(p,z), \quad (7)$$

$$\omega_u(p,z)=\omega_2/\cos\bar{\phi}(p,z), \quad (8)$$

and

$$\cos\bar{\phi}(p,z)=\sqrt{1-\bar{c}^2(z)p^2}. \quad (9)$$

Here $\bar{c}(z)$ is the depth-dependent background velocity [i.e., a smoothed version of the actual velocity function $c(z)$ (see, e.g., Figure 19 in a later section)]. This imaging procedure is not restricted to horizontally layered media; it can also be applied, for example, in a dipping target zone below a laterally varying overburden. We illustrate this with a numerical example (van Geloven and Wapenaar, 1996) for the configuration

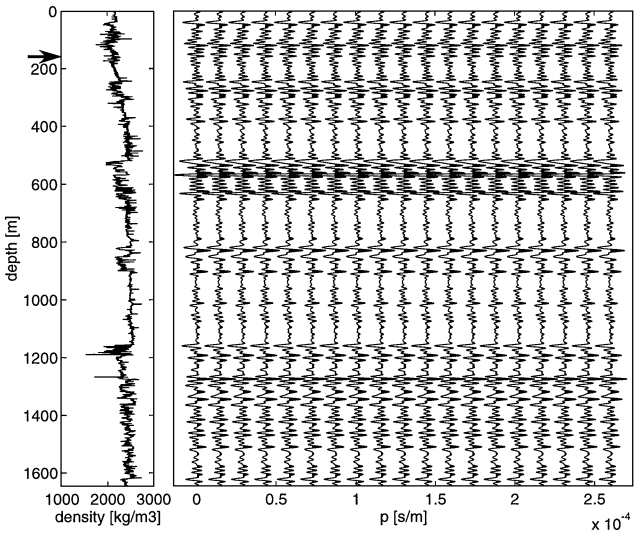

FIG. 6. Reflectivity section obtained with 1-D angle-dependent migration including the modified imaging step [equation (3)]. Note that the apparent AVA has been removed.

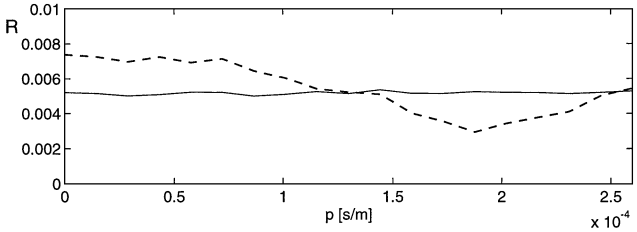

FIG. 7. Amplitude cross-section at $z=157$ m in Figure 6 (solid), compared with the result of Figure 3 (dashed).

shown in Figure 8; the velocity log of the finely layered target zone is shown in Figure 9. We modeled 400 shot records with a hybrid modeling scheme (wavenumber domain modeling in the target, including internal multiples, followed by an inverse Fourier transform and ray tracing through the overburden). Four of these shot records are shown in Figure 10. We redatumed these data in the space-frequency domain to a dipping reference level at the top of the target zone. Next, we applied a Radon transform to the redatumed shot record at lateral position $x_s = 3000$ m, and proceeded with 1-D angle-dependent migration along a single line normal to the target (marked z' in Figure 8. The results are shown in Figure 11. Figure 11a represents the true angle-dependent target reflectivity, convolved with an angle-independent spatial wavelet; this section serves as a reference. Figure 11b is the result of standard imaging (i.e., with fixed ω_ℓ and ω_u), and Figure 11c is the result of modified imaging according to equation (5). Figure 11d contains amplitude cross-sections of these results, picked in a small interval around $z' = 155$ m. Note that the result of modified imaging according to equation (5) (dashed line) matches the reference curve (solid line) significantly more accurately than the standard imaging result (dotted line).

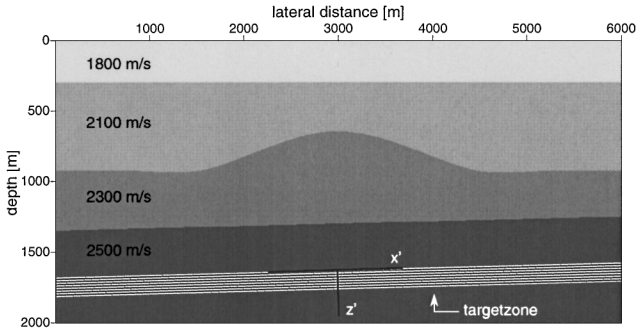

FIG. 8. Two-dimensional variable velocity model: a dipping finely layered target zone below a 2-D inhomogeneous overburden.

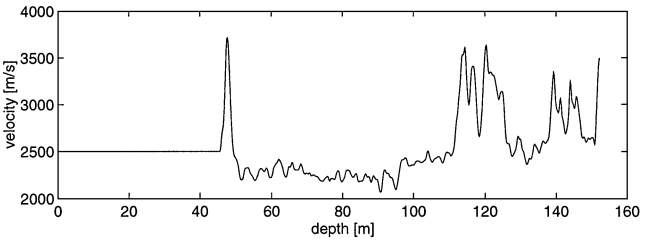

FIG. 9. Velocity log for the target zone. The "depth" is measured along the axis marked with z' in Figure 8, with $z' = 0$ at the top of the target.

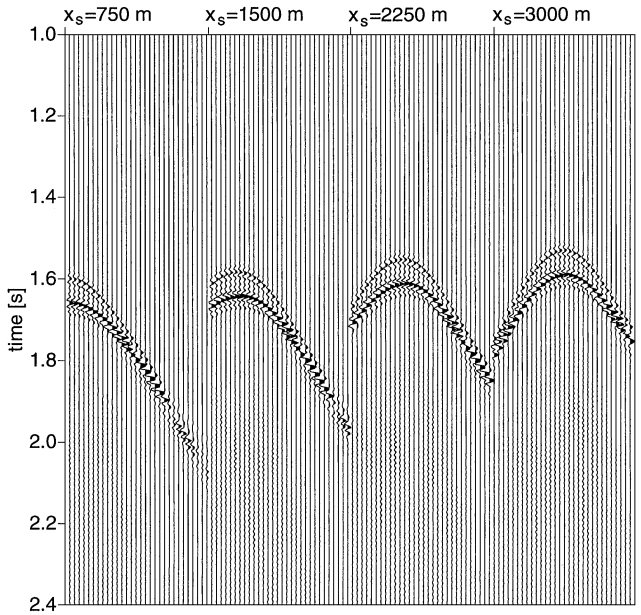

FIG. 10. Four shot records obtained by hybrid modeling (central frequency $f_c = 40$ Hz).

PROPAGATION-RELATED AVA EFFECTS OF FINE-LAYERING

In the previous section, we saw that the reflection-related apparent AVA effects of fine layering (i.e., angle-dependent interference) can be compensated by employing angle-dependent integration limits in the imaging integral [equation (3) or (5)].

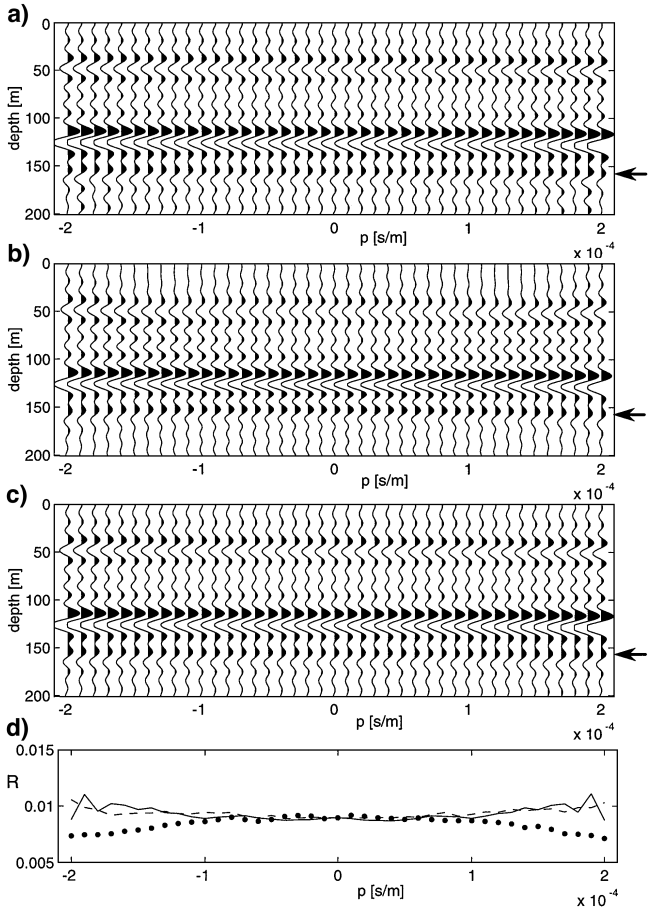

FIG. 11. Angle-dependent bandlimited reflectivity sections for the target zone. (a) Reference section. (b) Result of redatuming and migration, using standard imaging. (c) The same as (b), but imaging according to equation (5). (d) Maximum amplitudes, picked in a small depth interval around $z' = 155$ m [solid: (a), dotted: (b), dashed: (c)].

In our analysis, we considered primary reflection data; hence, the propagation-related apparent AVA effects were not considered. In this section, we investigate the latter effects with a numerical example.

We consider a horizontally layered, variable velocity, constant density medium. The velocity log $c(z)$ is shown in Figure 12. This figure also shows a reference section that has been obtained by convolving the true angle-dependent reflectivity section $\tilde{R}(p, z)$ with an angle-independent spatial wavelet $b(z)$, as in equation (4). Note that this reference section is muted at $p = \sin\bar{\phi}_{max}/\bar{c}(z)$, with $\bar{\phi}_{max} = 40^\circ$, which is the maximum angle that will be considered in the migration experiments. The plane-wave reflection response of the velocity log in Figure 12, including all internal multiple reflections, is shown in the (p, τ)-domain in Figure 13. We applied 1-D angle-dependent primary migration, using the imaging step described by equation (5). For $p = 0$, the bandwidth is reduced approximately by a factor $\cos\bar{\phi}_{max} \approx 0.77$, which means that the resolution loss for vertical propagation is approximately 23%. The result is shown in Figure 14, and the difference with the reference section is shown in Figure 15. Note that this difference section contains significant angle-dependent errors, despite the fact that we corrected for the reflection-related apparent AVA effects [equation (5)]. These errors are due to the fact that the primary downward extrapolation operators do not account for the angle-dependent dispersion effects related to the fine layering.

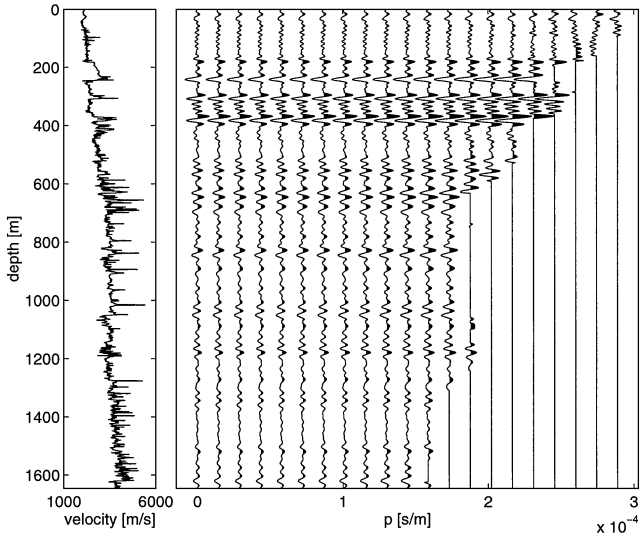

FIG. 12. Velocity log and angle-dependent band-limited reflectivity section. This section serves as a reference for the migration experiments.

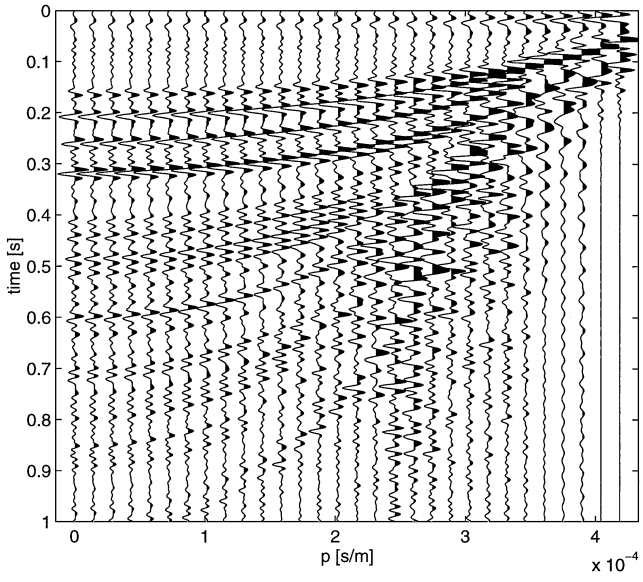

FIG. 13. Plane-wave reflection response, including all internal multiples (modeled with the reflectivity method, using a zero-phase wavelet with $f_c = 40$ Hz).

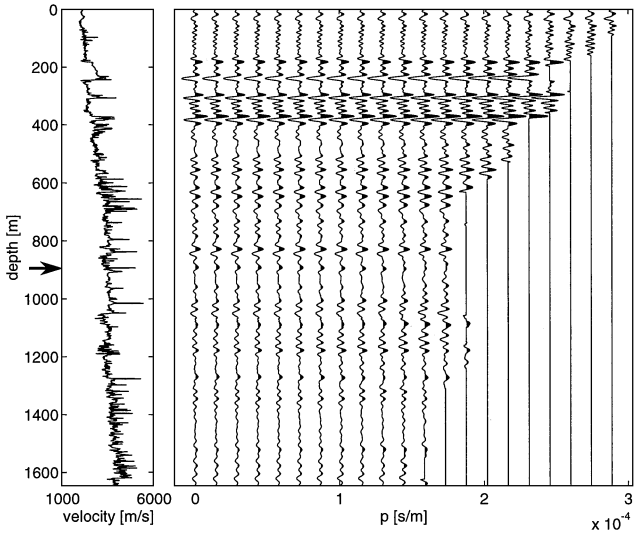

FIG. 14. Result of primary migration using the modified imaging step [equation (5)].

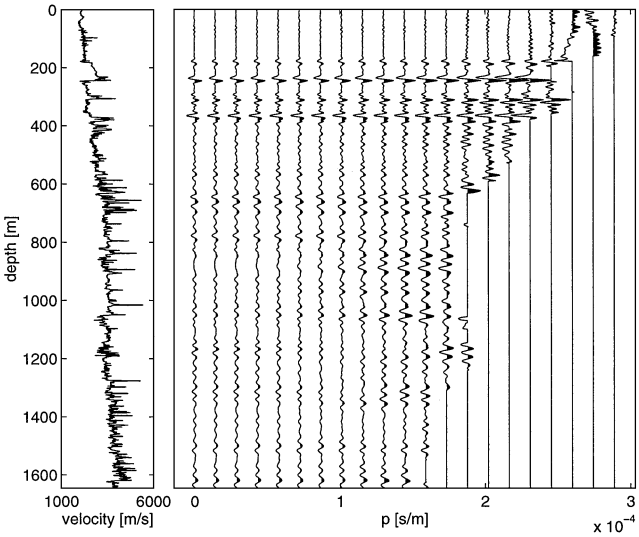

FIG. 15. Difference with the reference section. The amplitudes are plotted with the same gain as in Figures 12 and 14.

Compensating for propagation-related apparent AVA

The plane-wave reflection response of a horizontally layered medium, including all internal multiples, is fully captured by the generalized primary representation (Hubral et al., 1980; Resnick et al., 1986; Wapenaar, 1996):

$$\tilde{P}(p, z_0, \omega) = \int_{z_0}^{\infty} \tilde{W}_g^-(p, z_0, z, \omega)\tilde{R}(p, z)\tilde{W}_g^+(p, z, z_0, \omega)S(\omega)\,\mathrm{d}z. \quad (10)$$

Here, $\tilde{W}_g^+(p, z, z_0, \omega)$ and $\tilde{W}_g^-(p, z_0, z, \omega)$ are the generalized primary propagators which describe the plane-wave transmission responses of the finely layered medium between depth levels z_0 and z, including all internal multiple reflections in this region (Anstey and O'Doherty, 1971; Ursin, 1987; Herrmann and Wapenaar, 1992; Stanke and Burridge, 1993; Shapiro et al., 1994). Using flux-normalization, we have $\tilde{W}_g^-(p, z_0, z, \omega) = \tilde{W}_g^+(p, z, z_0, \omega)$. Wapenaar and Herrmann (1993) showed how to invert these propagators in a stable manner; a slightly different procedure was used by Widmaier et al., (1996).

True amplitude migration, based on the generalized primary representation (10), involves downward extrapolation, according to

$$\tilde{P}(p, z, \omega) = \tilde{F}_g^-(p, z, z_0, \omega)\tilde{P}(p, z_0, \omega)\tilde{F}_g^+(p, z_0, z, \omega), \quad (11)$$

($\tilde{F}_g^{\pm}$ is the inverse of $\tilde{W}_g^{\pm}$), followed by imaging, according to equation (5). We refer to these two steps as "generalized primary migration." We applied these two steps to the data of Figure 13. The result is shown in Figure 16, and the difference with the reference section is shown in Figure 17. Note that this difference section shows significantly less residuals than the difference section of the primary migration result (Figure 15). The remaining residuals are mainly due to the fact that a smoothed velocity function $\bar{c}(z)$ (see Figure 19 in the next section) has been used in the imaging step [equations (5)–(9)].

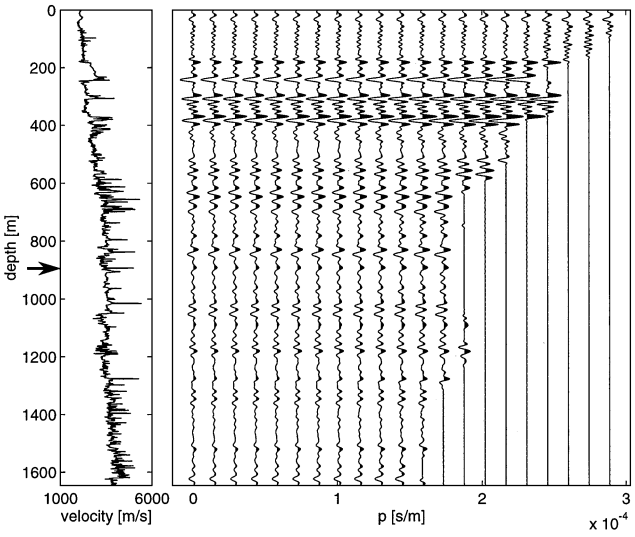

FIG. 16. Result of generalized primary migration according to equations (11) and (5).

Figure 18 contains amplitude cross-sections of Figures 12, 14, and 16 picked in a small interval around $z = 890$ m. Note that the angle-dependent reflectivity curve obtained with the generalized primary migration (the dashed line in Figure 18) matches the reference curve (the solid line) very well.

EXTENSION TO ELASTIC MEDIA

For elastic media, we modify the downward extrapolation step (equation 11) to

$$\tilde{P}_{\alpha,\beta}(p, z, \omega) \approx \tilde{F}_{g,\alpha}^-(p, z, z_0, \omega)\tilde{P}_{\alpha,\beta}(p, z_0, \omega)\tilde{F}_{g,\beta}^+(p, z_0, z, \omega), \quad (12)$$

where $\tilde{P}_{\alpha,\beta}(p, z_0, \omega)$ represents the decomposed multicomponent reflection data at the acquisition surface z_0 after surface related multiple elimination (this equation is an approximation because only one data type is included in its righthand side). The subscripts α and β refer to the wave type; each of these subscripts may stand for P- or S-waves. Moreover, $\tilde{F}_{g,\alpha}^{\pm}$ is the inverse of $\tilde{W}_{g,\alpha}^{\pm}$, where $\tilde{W}_{g,\alpha}^{\pm}$ is the α-wave generalized primary propagator for the finely-layered elastic medium (Burridge and Chang, 1989; de Hoop, 1991; de Hoop et al., 1991; Kohler et al., 1996a,b; Shapiro et al., 1996). Using flux normalization, we have $\tilde{W}_{g,\alpha}^- = \tilde{W}_{g,\alpha}^+$ and, consequently, $\tilde{F}_{g,\alpha}^- = \tilde{F}_{g,\alpha}^+$. Wapenaar (1996) discusses how to obtain these inverse propagators in a stable manner.

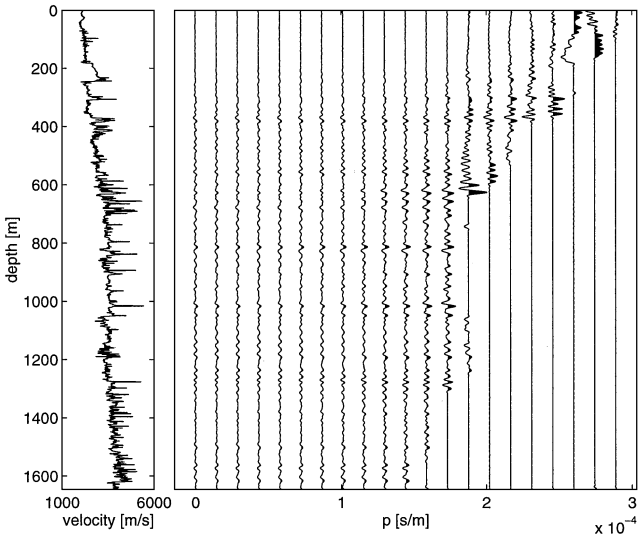

FIG. 17. Difference with the reference section. The amplitudes are plotted with the same gain as in Figures 12 and 16.

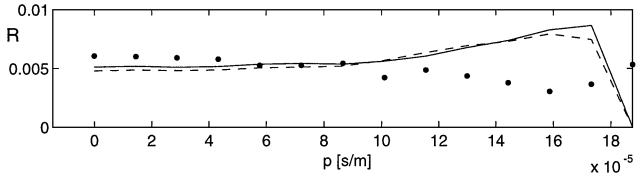

FIG. 18. Picked maximum amplitudes in a small depth interval around $z = 890$ m in Figures 12 (solid), 14 (dotted), and 16 (dashed).

The imaging step (equation 5) is modified to

$$\langle \tilde{R}_{\alpha,\beta}(p,z)\rangle = \frac{\mathcal{C}_{\alpha,\beta}(p,z)}{\pi}\Re\int_{\omega_\ell(p,z)}^{\omega_u(p,z)}\left(\frac{\tilde{P}_{\alpha,\beta}(p,z,\omega)}{S_\beta(\omega)}\right)\mathrm{d}\omega, \tag{13}$$

with

$$\mathcal{C}_{\alpha,\beta}(p,z) = \frac{\cos\bar{\phi}_\alpha(p,z)}{\bar{c}_\alpha(z)} + \frac{\cos\bar{\phi}_\beta(p,z)}{\bar{c}_\beta(z)}, \tag{14}$$

$$\omega_\ell(p,z) = 2k_1/\mathcal{C}_{\alpha,\beta}(p,z), \tag{15}$$

$$\omega_u(p,z) = 2k_2/\mathcal{C}_{\alpha,\beta}(p,z), \tag{16}$$

and

$$\cos\bar{\phi}_\alpha(p,z) = \sqrt{1-\bar{c}_\alpha^2(z)p^2}. \tag{17}$$

Here, $\bar{c}_\alpha(z)$ is the α-wave propagation velocity of the background model; the wavenumbers k_1 and k_2 can be chosen freely, with the constraint that $\omega_\ell(p,z)$ and $\omega_u(p,z)$ do not exceed the temporal band limits of the β-wave source function $S_\beta(\omega)$. Optionally, a replacement source function $S_r(\omega\mathcal{C}_{\alpha,\beta}(p,z))$ can be inserted under the integral in equation (13) in order to suppress the artifacts of the division by $S_\beta(\omega)$. In Appendix A, it is shown that for the simplified situation of "primaries only" and a homogeneous macro velocity model, equations (12) through (17) imply that the imaged reflectivity section $\langle\tilde{R}_{\alpha,\beta}(p,z)\rangle$ can be written as the true reflectivity section $\tilde{R}_{\alpha,\beta}(p,z)$, convolved with an angle-independent spatial wavelet $b(z)$, according to

$$\langle\tilde{R}_{\alpha,\beta}(p,z)\rangle = b(z) * \tilde{R}_{\alpha,\beta}(p,z) \tag{18}$$

(equation A-6). We will show with a numerical example that this relation holds approximately true for the generalized primary migration result in a variable velocity elastic medium (van Geloven and Wapenaar, 1997). Figure 19 shows P- and S-wave velocity logs [$c_P(z)$ and $c_S(z)$] and their smoothed versions [$\bar{c}_P(z)$ and $\bar{c}_S(z)$] to be used in equations (13) through (17); the density is chosen to be constant.

Figure 20 shows the reference sections, which have been obtained by convolving the true reflectivity sections $\tilde{R}_{\alpha,\beta}(p,z)$ with an angle-independent spatial wavelet. The exact elastic plane-wave reflection responses (including internal multiples and conversions) of the logs $c_P(z)$ and $c_S(z)$ in Figure 19 are shown in the (p,τ)-domain in Figure 21. The results of elastic generalized primary migration according to equations (12) and (13) are shown in Figure 22. Figure 23 shows the differences with the reference sections in Figure 20. Note that the residues are again very small (their magnitude is of the same order as in Figure 17).

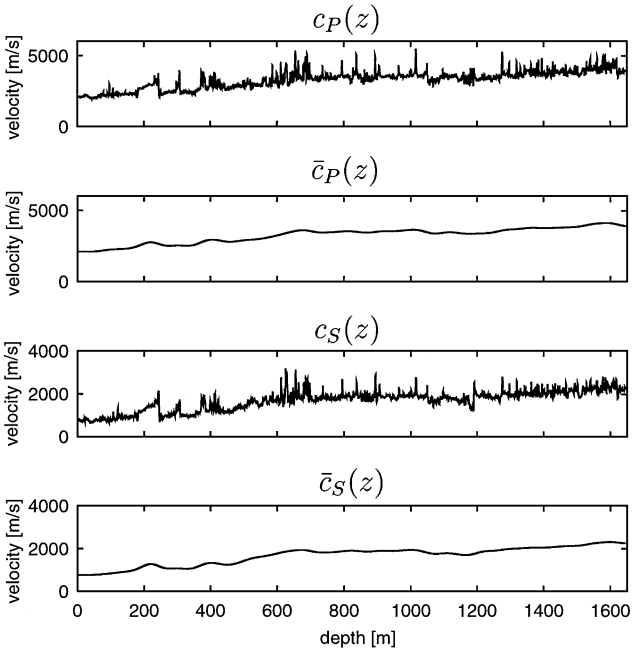

FIG. 19. P- and S-wave velocity logs [$c_P(z)$ and $c_S(z)$] used for forward modeling, and smoothed logs [$\bar{c}_P(z)$ and $\bar{c}_S(z)$] that serve as background models in the imaging step.

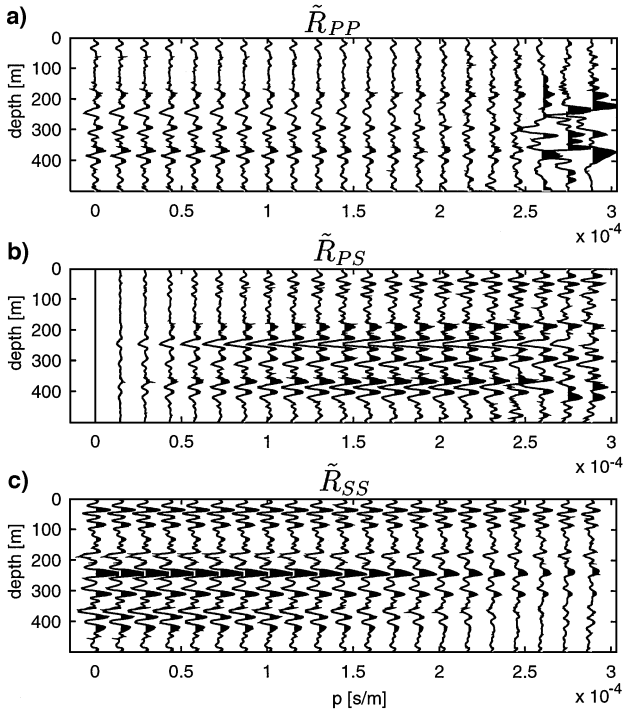

FIG. 20. Band-limited reflectivity sections, which serve as references for the migration experiment.

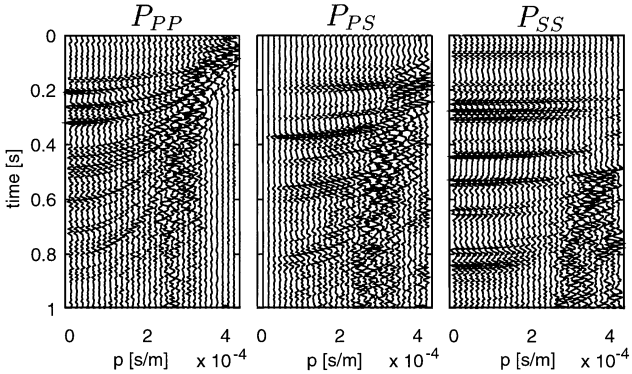

FIG. 21. Plane-wave reflection responses (including internal multiples and conversions) of the logs $c_P(z)$ and $c_S(z)$ in Figure 19 (modeled with the reflectivity method).

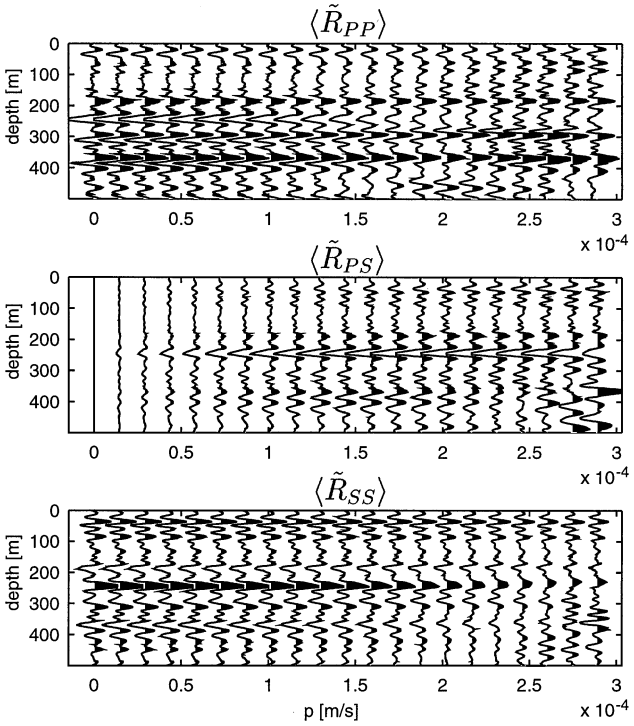

FIG. 22. Results of elastic generalized primary migration according to equations (12) and (13).

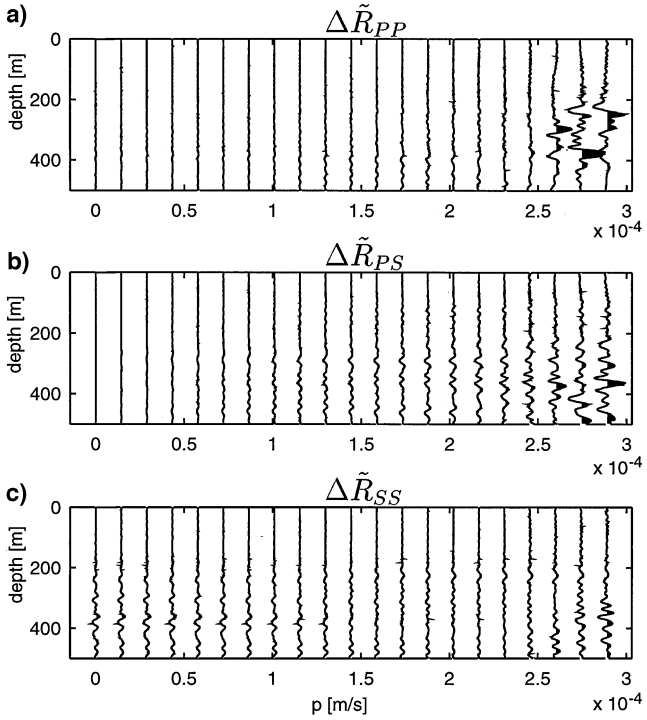

FIG. 23. Differences with the reference sections. The amplitudes are plotted with the same gain as in Figures 20 and 22.

CONCLUSIONS

The apparent AVA effects due to fine layering can be subdivided into reflection- and propagation-related effects.

Reflection-related apparent AVA effects

The reflection of a package of thin layers is accompanied with wavelet interference. Since, for a given frequency, the vertical wavelength varies with the angle of incidence, the interference effects are also angle dependent. Due to the band limitation of seismic data, the interference effects cannot be removed. However, we have proposed a filter that equalizes these effects. This filter can be integrated in the imaging step in migration. In this way, migration yields a band-limited reflectivity section without reflection-related apparent AVA. The underlying assumption is that the source function is known and that source directivity effects have been compensated prior to migration.

Propagation-related apparent AVA effects

The propagation through a package of thin layers is accompanied with wavelet dispersion. This dispersion is caused by internal multiple scattering and depends also on the propagation angle. It is quantified by the generalized primary propagator. The inverse of this propagator can be used in the downward extrapolation step in migration. Combined with the filter mentioned above, migration yields in this way a band-limited reflectivity section in which the apparent AVA effects of fine layering are suppressed.

We have demonstrated the effect of these two modifications with numerical examples. In all cases we observed a significant improvement of the imaged AVA sections. From these sections, the band-limited medium parameters can be resolved by local AVA inversion (van Wijngaarden, 1998).

ACKNOWLEDGMENT

The authors thank the Dutch Technology Foundation (STW) and the sponsors of the DELPHI consortium for their financial support.

REFERENCES

Anstey, N. A., and O'Doherty, R. F., 1971, Reflections on amplitudes: Geophys. Props., **19**, 430–458.
Burridge, R., and Chang, H. W., 1989, Multimode, one-dimensional wave propagation in a highly discontinuous medium: Wave Motion, **11**, 231–249.
Clayton, R. W., and McMechan, G. A., 1981, Inversion of refraction data by wave field continuation: Geophysics, **46**, 860–868.
de Haas, J. C., and Berkhout, A. J., 1990, Local inversion of PP, PS, SP and SS reflections: 60th Annual Internat. Mtg., Soc. Expl. Geophys., Expanded Abstracts, 1189–1192.
de Hoop, M. V., 1991, Wave propagation with tunneling in a highly discontinuous layered medium: Wave Motion, **13**, 307–327.
de Hoop, M. V., Chang, H. W., and Burridge, R., 1991, The pseudo-primary field due to a point-source in a finely layered medium: Geophys. J. Internat., **104**, 489–506.
Herrmann, F. J., and Wapenaar, C. P. A., 1992, Macro description of fine layering: A proposal for an extended macro model: 62nd Annual Internat. Mtg., Soc. Expl. Geophys., Expanded Abstracts, 1263–1266.
Hubral, P., Treitel, S., and Gutowski, P. R., 1980, A sum autoregressive formula for the reflection response: Geophysics, **45**, 1697–1705.
Kohler, W., Papanicolaou, G., and White, B., 1996a, Localization and mode conversion for elastic waves in randomly layered media I: Wave Motion, **23**, 1–22.
——— 1996b, Localization and mode conversion for elastic waves in randomly layered media II: Wave Motion, **23**, 181–201.
Ostrander, W. J., 1984, Plane-wave reflection coefficients for gas sands at nonnormal angles of incidence: Geophysics, **49**, 1637–1648.

Prein, R. J., and Verschuur, D. J., 1997, Estimation of the effective source wave field by surface-related multiple elimination: 67th Annual Internat. Mtg., Soc. Expl. Geophys., Expanded Abstracts, 1406–1409.
Resnick, J. R., Lerche, I., and Shuey, R. T., 1986, Reflection, transmission, and the generalized primary wave: Geophys. J. Roy. Astr. Soc., **87**, 349–377.
Shapiro, S. A., Hubral, P., and Ursin, B., 1996, Reflectivity/transmissivity for one-dimensional inhomogeneous random elastic media: Dynamic-equivalent-medium approach: Geophys.. J. Internat., **126**, 184–196.
Shapiro, S. A., Hubral, P., and Zien, H., 1994, Frequency-dependent anisotropy of scalar waves in a multilayered medium: J. Seismic Expl., **3**, 37–52.
Stanke, F. E., and Burridge, R., 1993, Spatial versus ensemble averaging for modeling wave propagation in finely layered media: J. Acoust. Soc. Am., **93**, no. 1, 36–41.
Swan, H. W., 1991, Amplitude-versus-offset measurement errors in a finely layered medium: Geophysics, **56**, 41–49.
———1997, Removal of offset-dependent tuning in AVO analysis: 67th Ann. Internat. Mtg., Soc. Expl. Geophys., Expanded Abstracts, 175–178.
Ursin, B., 1987, The plane-wave reflection and transmission response of a vertically inhomogeneous acoustic medium, *in* Bernabini, M., Carrion, P., Jacovitti, G., Rocca, F., Treitel, S., and Worthington, M., Eds., Deconvolution and inversion: Blackwell Scientific Publications, 189–207.
van Geloven, W. J. F., and Wapenaar, C. P. A., 1996, Improved AVA imaging in laterally varying media: 66th Ann. Internat. Mtg., Soc. Expl. Geophys., Expanded Abstracts, 1723–1726.
———1997, Elastic imaging in finely layered media: 67th Ann. Internat. Mtg., Soc. Expl. Geophys., Expanded Abstracts, 142–145.
van Wijngaarden, A. J., 1998, Imaging and characterization of angle-dependent seismic reflection data: Ph.D. thesis, Delft University of Technology.
van Wijngaarden, A. J., and Wapenaar, C. P. A., 1995, Residue analysis in linearized elastic inversion: 65th Ann. Internat. Mtg., Soc. Expl. Geophys., Expanded Abstracts, 647–650.
Verschuur, D. J., Berkhout, A. J., and Wapenaar, C. P. A., 1992, Adaptive surface-related multiple elimination: Geophysics, **57**, 1166–1177.
Wapenaar, C. P. A., 1996, One-way representations of seismic data: Geophys. J. Internat., **127**, 178–188.
Wapenaar, C. P. A., and Herrmann, F. J., 1993, True amplitude migration taking fine-layering into account: 63rd Ann. Internat. Mtg., Soc. Expl. Geophys., Expanded Abstracts, 653–656.
Widmaier, M. T., Shapiro, S. A., and Hubral, P., 1996, AVO correction for scalar waves in the case of a thinly layered reflector overburden: Geophysics, **61**, 520–528.

APPENDIX A

ANALYSIS OF THE ANGLE-DEPENDENT IMAGING INTEGRALS

We analyze the p-dependent imaging integral [equation (13)] for the elastic situation. For this analysis, we consider the primary reflection response of a horizontally layered elastic medium, and we indicate how the results simplify for the acoustic situation. Throughout this appendix we assume a homogeneous macro model. The generalizations for more realistic situations are discussed in the sections "Extension to acoustic variable-velocity media" and "Extension to elastic media."

Assuming a homogeneous macro model, the elastic primary reflection response of a continuous finely layered medium in the half-space $z > z_0$ reads in the raypath parameter–frequency (p, ω) domain

$$\tilde{P}_{\alpha,\beta}(p, z_0, \omega) = \int_{z_0}^{\infty} \tilde{W}_{\alpha}^{-}(p, z_0, z, \omega)\tilde{R}_{\alpha,\beta}(p, z)\tilde{W}_{\beta}^{+}(p, z, z_0, \omega)S_{\beta}(\omega)\,\mathrm{d}z. \tag{A-1}$$

The subscripts α and β refer to the wave type; each of these subscripts may stand for P- or S-waves. From right to left, $S_{\beta}(\omega)$ is the source function, $\tilde{W}_{\beta}^{+}(p, z, z_0, \omega)$ is the primary propagator for downgoing β-waves, $\tilde{R}_{\alpha,\beta}(p, z)$ is the reflection function that transforms downgoing β-waves into upgoing α-waves, and $\tilde{W}_{\alpha}^{-}(p, z_0, z, \omega)$ is the primary propagator for upgoing α-waves. Since we consider a homogeneous macro model, these propagators read

$$\tilde{W}_{\alpha}^{-}(p, z_0, z, \omega) = \tilde{W}_{\alpha}^{+}(p, z, z_0, \omega) = \exp\{j\omega(z_0 - z)\,q_{\alpha}\}, \tag{A-2}$$

where q_{α} is the vertical α-wave slowness, according to $q_{\alpha} = (\cos\phi_{\alpha})/c_{\alpha}$, with $\cos\phi_{\alpha} = \sqrt{1 - c_{\alpha}^2 p^2}$, c_{α} being the α-wave propagation velocity of the macro model.

For propagating waves (i.e., for real-valued vertical slownesses), angle-dependent migration involves downward extrapolation to depth level z, according to

$$\tilde{P}_{\alpha,\beta}(p, z, \omega) = \tilde{F}_{\alpha}^{-}(p, z, z_0, \omega)\tilde{P}_{\alpha,\beta}(p, z_0, \omega)\tilde{F}_{\beta}^{+}(p, z_0, z, \omega), \tag{A-3}$$

($\tilde{F}_{\alpha}^{\pm}$ is the inverse of $\tilde{W}_{\alpha}^{\pm}$), followed by imaging, according to

$$\langle\tilde{R}_{\alpha,\beta}(p, z)\rangle = \frac{\mathcal{C}_{\alpha,\beta}(p)}{\pi}\Re\int_{\omega_{\ell}(p)}^{\omega_u(p)} S_r(\omega\mathcal{C}_{\alpha,\beta}(p))\left(\frac{\tilde{P}_{\alpha,\beta}(p, z, \omega)}{S_{\beta}(\omega)}\right)\mathrm{d}\omega, \tag{A-4}$$

where $\Re$ denotes that the real part is taken and $\langle\cdot\rangle$ denotes a band-limited estimate; $S_r(\omega\mathcal{C}_{\alpha,\beta}(p))$ is an optional replacement source function. Our aim is to derive expressions for the lower and upper integration limits $\omega_{\ell}(p)$ and $\omega_u(p)$ and for the factor $\mathcal{C}_{\alpha,\beta}(p)$ so that the spatial bandwidth of $\langle\tilde{R}_{\alpha,\beta}(p, z)\rangle$ is independent of the raypath parameter p.

From equations (A-1)–(A-3), we obtain

$$\tilde{P}_{\alpha,\beta}(p, z, \omega) = \int_{z_0}^{\infty} \exp\{j\omega(z - z')(q_{\alpha} + q_{\beta})\}\tilde{R}_{\alpha,\beta}(p, z')S_{\beta}(\omega)\,\mathrm{d}z'. \tag{A-5}$$

Substitution of this result into equation (A-4) and interchanging the integrals yields

$$\langle\tilde{R}_{\alpha,\beta}(p, z)\rangle = \int_{z_0}^{\infty} b(z - z')\tilde{R}_{\alpha,\beta}(p, z')\,\mathrm{d}z', \tag{A-6}$$

where

$$b(z) = \frac{\mathcal{C}_{\alpha,\beta}(p)}{\pi}\Re\int_{\omega_{\ell}(p)}^{\omega_u(p)} S_r(\omega\mathcal{C}_{\alpha,\beta}(p)) \times \exp\{j\omega z(q_{\alpha} + q_{\beta})\}\,\mathrm{d}\omega. \tag{A-7}$$

The right side in equation (A-6) represents a spatial convolution along the z-axis. We will show that the spatial wavelet $b(z)$ is independent of p when we choose

$$\mathcal{C}_{\alpha,\beta}(p) = q_\alpha + q_\beta = \frac{\cos\phi_\alpha(p)}{c_\alpha} + \frac{\cos\phi_\beta(p)}{c_\beta}, \quad \text{(A-8)}$$

$$\omega_\ell(p) = 2k_1/\mathcal{C}_{\alpha,\beta}(p), \quad \text{(A-9)}$$

and

$$\omega_u(p) = 2k_2/\mathcal{C}_{\alpha,\beta}(p). \quad \text{(A-10)}$$

Here, the wavenumbers k_1 and k_2 can be chosen freely, with the constraint that $\omega_\ell(p)$ and $\omega_u(p)$ do not exceed the temporal band limits of the source function $S_\beta(\omega)$. Substituting equations (A-8)–(A-10) into equation (A-7) and replacing the integration variable ω by $k_z = \omega\mathcal{C}_{\alpha,\beta}(p)$ yields

$$b(z) = \frac{1}{\pi}\Re\int_{2k_1}^{2k_2} S_r(k_z)\exp(jk_z z)\,\mathrm{d}k_z. \quad \text{(A-11)}$$

Hence, $b(z)$ is indeed independent of the raypath parameter p; it simply denotes the inverse Fourier transform of the replacement source function $S_r(k_z)$ (assuming its bandwidth does not exceed the limits $2k_1$ and $2k_2$). When this replacement source function is omitted, we obtain

$$b(z) = \frac{\sin 2k_2 z}{\pi z} - \frac{\sin 2k_1 z}{\pi z}. \quad \text{(A-12)}$$

Finally, note that for the acoustic situation, equations (A-8)–(A-10) simplify to

$$\mathcal{C}(p) = \frac{2\cos\phi(p)}{c}, \quad \text{(A-13)}$$

$$\omega_\ell(p) = \omega_1/\cos\phi(p), \quad \text{(A-14)}$$

and

$$\omega_u(p) = \omega_2/\cos\phi(p), \quad \text{(A-15)}$$

where ω_1 and ω_2 are related to k_1 and k_2, according to $\omega_1 = k_1 c$ and $\omega_2 = k_2 c$.